Chapter 4

Characteristics of Time Dependent Vortex Flow

It is observed in the present experiment that the vortex flow in the processing chamber does not reach steady state at long time when the buoyancy-to-inertia ratio Gr/Re_j^2 is raised to certain high level and the vortex flow gradually becomes time dependent. This normally occurs at low jet Reynolds numbers for the range of the Rayleigh number covered here. Besides, the transient stages during the formation of the inertia-driven vortex rolls are of interest in the fundamental fluid mechanics and heat transfer study. In this chapter these two different time dependent vortex flows will be examined in detail.

4.1 Time periodic vortex flows

The characteristics of a typical buoyancy-driven time periodic vortex flow are exemplified first in Fig. 4.1 for two cases with D_j=10.0 and 22.1 mm by showing selected cross plane flow photos at certain time instants and time records of air temperature at selected locations in the processing chamber in the statistical state for H=20.0 mm. We should first recall that at low Re_j only the primary inertia-driven inner and buoyancy-driven outer vortex rolls exist in the chamber. The secondary inertia-driven middle roll does not appear. Now the results in Fig. 4.1 clearly show that two additional circular rolls are induced in the time periodic vortex flow. These two new rolls are smaller and appear in the middle portion of the chamber right between the inner and outer rolls. Besides, the time periodic vortex flow is asymmetric. The data for the time records given in Fig. 4.1 indicate that only in the region dominated by the new rolls the air temperature oscillates significantly with time. Elsewhere the temperature oscillation is small. It is recognized that for the

smaller H of 10.0 and 15.0 mm the Rayleigh number of the flow subject to the ΔT investigated here is not high enough to cause the vortex flow to become time dependent at long time. Therefore at H=10.0 and 15.0 mm the vortex flow for various cases all evolves to steady state.

To further reveal the temporal characteristics of the time periodic vortex flow, the time records of the air temperature at a selected location and the corresponding power spectrum densities (PSD) are presented next in Fig. 4.2 for various Re_j for D_j=22.1 mm at Ra=15,030. The PSD are evaluated from the Fourier analysis of the measured data. The results clearly manifest that the flow oscillates at a large amplitude and a slightly lower frequency for a lower Re_j at the fixed Ra. This trend is apparently owing to the accompanying rise in the buoyancy-to-inertia ratio at reducing Re_j. Note that the time periodic flow prevails over a finite noticeable range of the jet Reynolds number (Figs. 4.2(b)-(d)) and the flow oscillation is characterized by a single fundamental frequency. At certain low Re_j (high Gr/Re_j^2) the flow oscillation becomes quasi-periodic in time and second fundamental frequency sets in (Fig. 4.2(a)).

Then, the effects of the Rayleigh number on the temporal characteristics of the time periodic vortex flow are illustrated in Fig. 4.3 by showing the time histories of the air temperature at a selected location for various Ra at Re_j=61 for the large injection pipe. Note that the oscillation amplitude of the air temperature is only slightly affected by the variation in the Rayleigh number. The corresponding power spectrum densities also shown in Fig. 4.3 suggest that the flow oscillates at a slightly lower frequency for a higher Rayleigh number.

Based on the data from the present temperature measurement for H=20.0 mm, the oscillation frequency of the buoyancy-driven time periodic vortex flow in the processing chamber with the large injection pipe can be correlated as

$$F = \frac{f}{\left(\alpha / H^2\right)} = -0.231 + 0.0183\,\text{Re} + 5{,}450\,\text{Ra}^{-1} \qquad (4.1)$$

While for the small injection pipe

$$F = \frac{f}{\left(\alpha / H^2\right)} = 0.0203 + 0.0105\,\text{Re} - 6{,}050\,\text{Ra}^{-1} \qquad (4.2)$$

Both equations can predict our data with a standard deviation less than 5%.

It is of interest to explore the temporal evolution of the time periodic vortex flow. This is illustrated in Fig. 4.4 by showing the side view flow photos and the corresponding schematically sketched vortex flow patterns at the cross plane $\theta = 0°$ at selected time instants in a typical periodic cycle for the case with $\text{Re}_j=61$ and Ra=11,350 for D_j=22.1 mm. Note that in the beginning of the cycle designated as time t=0s we only have two big vortex rolls in the processing chamber, namely, the primary inertia-driven roll in the core region of the chamber and the buoyancy-driven roll near the chamber side. Shortly later at t=1s a weak and small thermal plume rises from the heated copper disk in the region below the outer portion of the primary inertia-driven roll, causing this portion of the roll to become elongated in the radial direction. The thermal plume then grows quickly with time and a slender neck is formed between the outer and main portions of the primary inertia-driven roll. As this process continues, it is observed that at t=3s the outer portion of the roll splits from the main portion of the roll and a new circular vortex roll is generated in the region between the two big rolls. For a further increase in time the new roll strengthens gradually. Meanwhile the thermal plume grows slowly and evolves into another new circular vortex roll, as evident from the flow photos at t=7 & 9s. Thus, two additional rolls appear and there are four circular rolls in the processing chamber in this period of time. It is important to note that as the process keeps going, the roll resulting from

the splitting of the inertia-driven roll begins to decay. Later the new roll evolving from the thermal plume decays quickly and at t=11s it becomes very small. At t=13s it is already very weak and nearly disappears. Finally at the end of the cycle at t=t_p=13.3s, the two new rolls disappear completely and we only have two big rolls in the chamber.

To reveal the complete picture of the complex time periodic vortex flow structure, the top view flow photos taken at the middle horizontal plane Z=0.5 along with the side view flow photos taken at the cross plane θ=0° for the typical case examined above are presented in Fig. 4.5 at selected time instants in a typical periodic cycle. The results clearly show that the vortex flow does not possess axisymmetry and exhibits significant circumferential variation. In fact, the cross sections of the two new rolls vary circumferentially to such a large degree that each roll is in the form of large connecting blobs. The blobs are essentially the flow recirculations and they connect with the adjacent blobs through narrow necks. Besides, the blobs in the same roll do not have the same size and circulation strength.
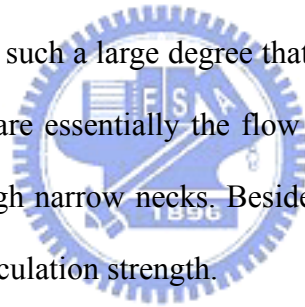
4.2 Flow regime map

Based on the present data, a flow regime map for the cases with H=20.0 mm delineating the temporal state of the inertia- and buoyancy-driven vortex flow in the processing chamber is shown in Fig. 4.6 in terms of the parameters chosen as Ra(D_j/H)$^{-0.3}$ vs. Re$_j$(D_j/H). The results in this plot manifest that when the jet Reynolds number Re$_j$ and/or the aspect ratio of the processing chamber D_j/H are high so that Re$_j$(D_j/H)$\geqq$200, the buoyancy-to-inertia ratio in the flow is low for the range of the Rayleigh number considered here and we have stable vortex flow. But when Re$_j$(D_j/H) is below 200, the vortex flow becomes time periodic as Ra(D_j/H)$^{-0.3}$ exceeds certain level. For a further raise in Ra the flow can evolve to a quasi-periodic state. Finally,

for a high buoyancy-to-inertia ratio the vortex flow shows a chaotic variation with time. More specifically, the boundary between the quasi-periodic and chaotic unstable vortex flow can be correlated as

$$Ra \times \left(\frac{D_j}{H}\right)^{-0.3} = 10700 + 10\left[Re_j \times \left(\frac{D_j}{H}\right)\right]^{1.5} \qquad (4.3)$$

In addition, the transitions from steady to time-periodic vortex flow occurs when

$$Ra \times \left(\frac{D_j}{H}\right)^{-0.3} = 2390 + 0.57\left[Re_j \times \left(\frac{D_j}{H}\right)\right]^{2} \qquad (4.4)$$

These two correlations are also shown in Fig. 4.6.

4.3 Formation of vortex flow

It is of interest to understand how the inertia-driven vortex rolls form during the transient stage following the jet impinging onto the heated disk. To investigate the formation of the inertia-driven rolls, the experiment is carried out by visualizing the vortex flow immediately after we start to inject the air into the processing chamber for an unheated disk (Ra=0). The instant we begin to inject the air is designated as time t=0. The side view flow photos at selected time instants for a few selected cases from this experiment are shown in Figs. 4.7 and 4.8. The results in Fig. 4.7(a) for a low jet Reynolds number for the small injection pipe indicate that shortly after the jet impingement at t=1s a small circular vortex roll forms around the jet axis in the inner zone of the processing chamber. The roll then gradually grows in size and strength at increasing time. Finally, at t≥ 40s the flow arrives at steady state. During the entire flow formation processes, only the primary inertia-driven roll is induced at this low Re_j of 136.

Next, the results shown in Fig. 4.7(b) for a much higher jet Reynolds number of 676 indicate that the vortex flow evolves at a much faster pace and at t=3s an

97

additional circular roll appears adjacent to the existing inner roll. The additional roll is known as "the secondary inertia-driven roll". In a short period of time the two rolls reach steady state at $t \geq 9s$.

Then, the flow formation in the chamber with the jet issued from the large injection pipe shown in Fig. 4.8 qualitatively resembles that in Fig. 4.7 for the small injection pipe. A close inspection of the results in Figs. 4.7 and 4.8, however, reveals that for the large injection pipe the jet Reynolds number is lower at the same Q_j, as evident from Equ. (3.1). Thus, the boundary layer in the wall-jet region over the disk is thicker and the induced rolls appear in the slightly upper region of the chamber. Finally, the time variations of the maximum radial extent of the primary inertia-driven roll and the location of the geometric center of the secondary inertia-driven roll are given in Figs. 4.9 and 4.10. The quick evolution of the rolls during the initial transient is noted.
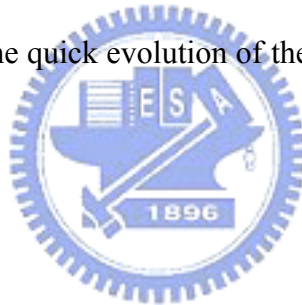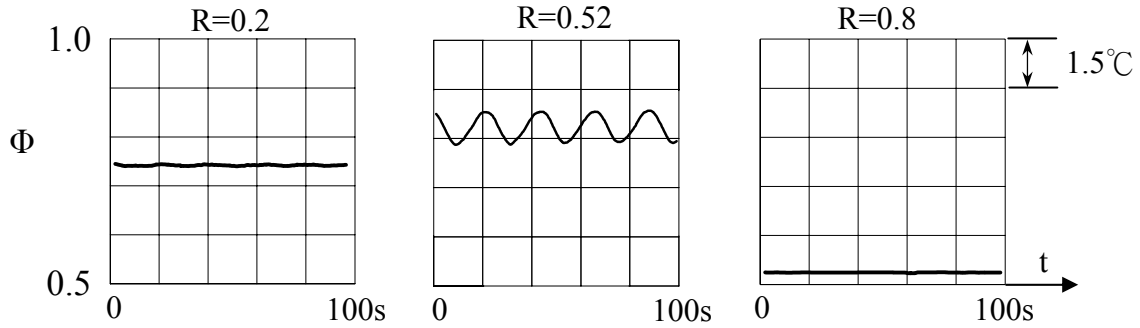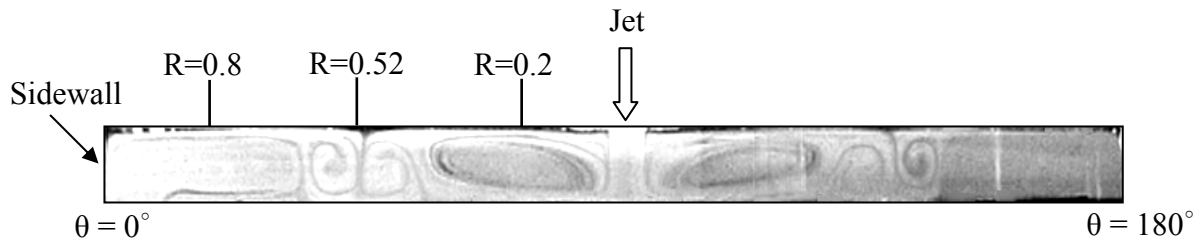
(a) $Re_j=136$, $Ra=11,270$ & $D_j=10.0$ mm ($Gr/Re_j^2=0.61$)
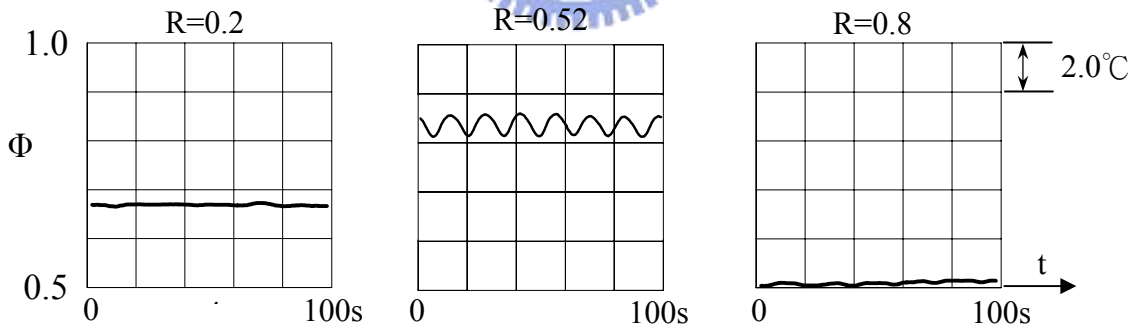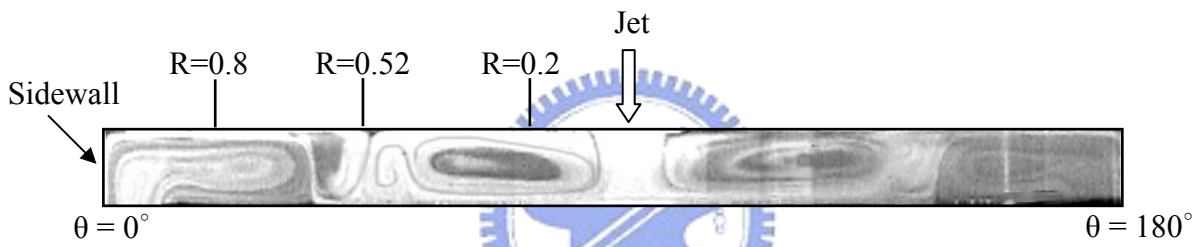
(b) $Re_j=61$, $Ra=15,030$ & $D_j=22.1$ mm ($Gr/Re_j^2=4.03$)

Fig. 4.1   Side view flow photos at the cross plane $\theta=0°$ & $180°$ at certain time instant in a typical periodic cycle and time records of air temperature at selected locations in the middle horizontal plane $Z=0.5$ with $H=20.0$ mm for (a) $Re_j=136$, $Ra=11,270$ & $D_j=10.0$ mm ($t_p=21.1$ sec) and (b) $Re_j=61$, $Ra=15,030$ & $D_j=22.1$ mm ($t_p=13.8$ sec).

99
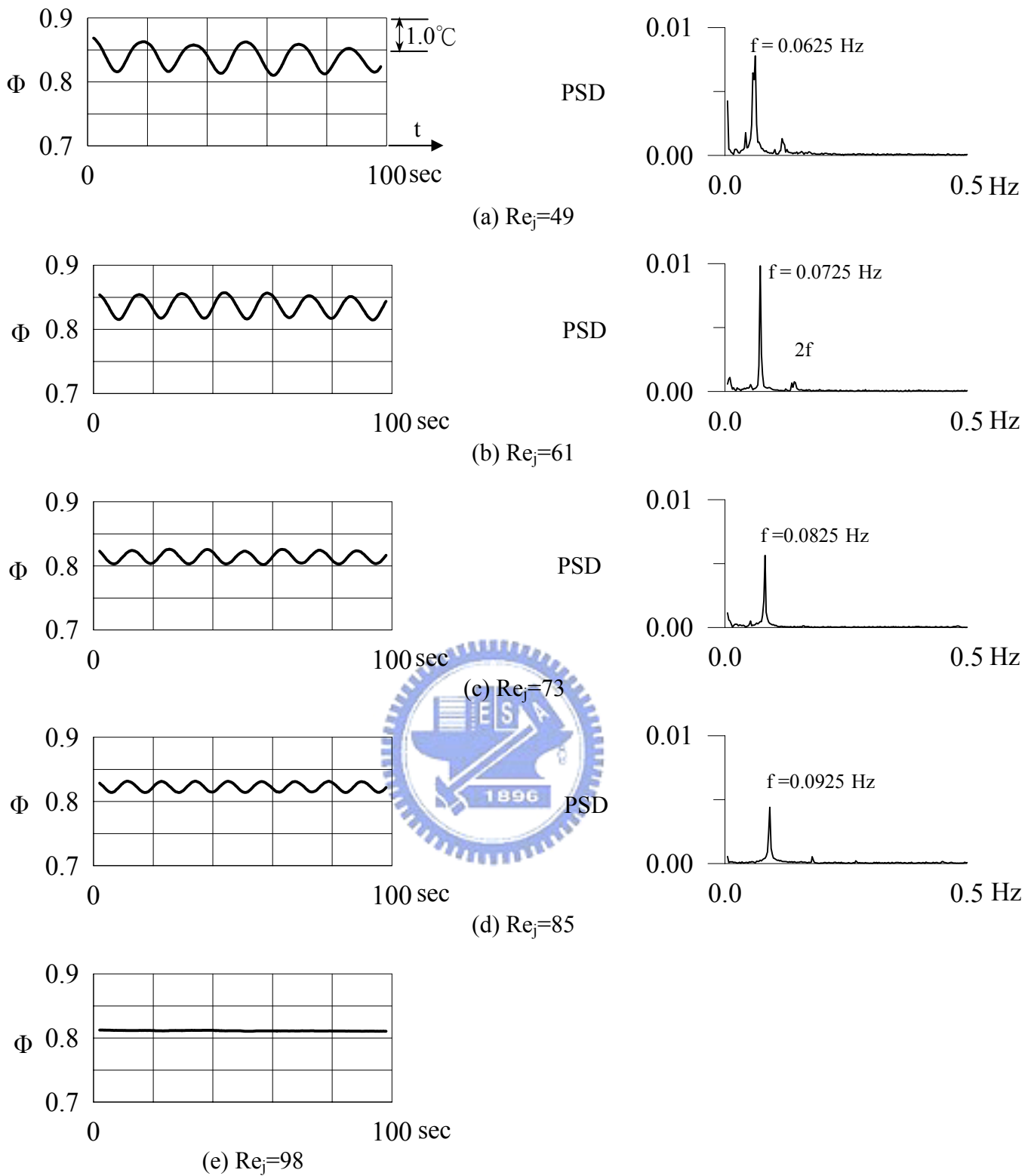
Fig. 4.2 The time records of non-dimensional air temperature and the corresponding power spectrum densities for Ra=15,030 and D_j=22.1 mm at location (R, Z) =(0.52, 0.5) for θ=0º with H=20.0 mm for various Reynolds numbers Re_j= (a)49, (b)61, (c)73, (d)85 and (e)98.
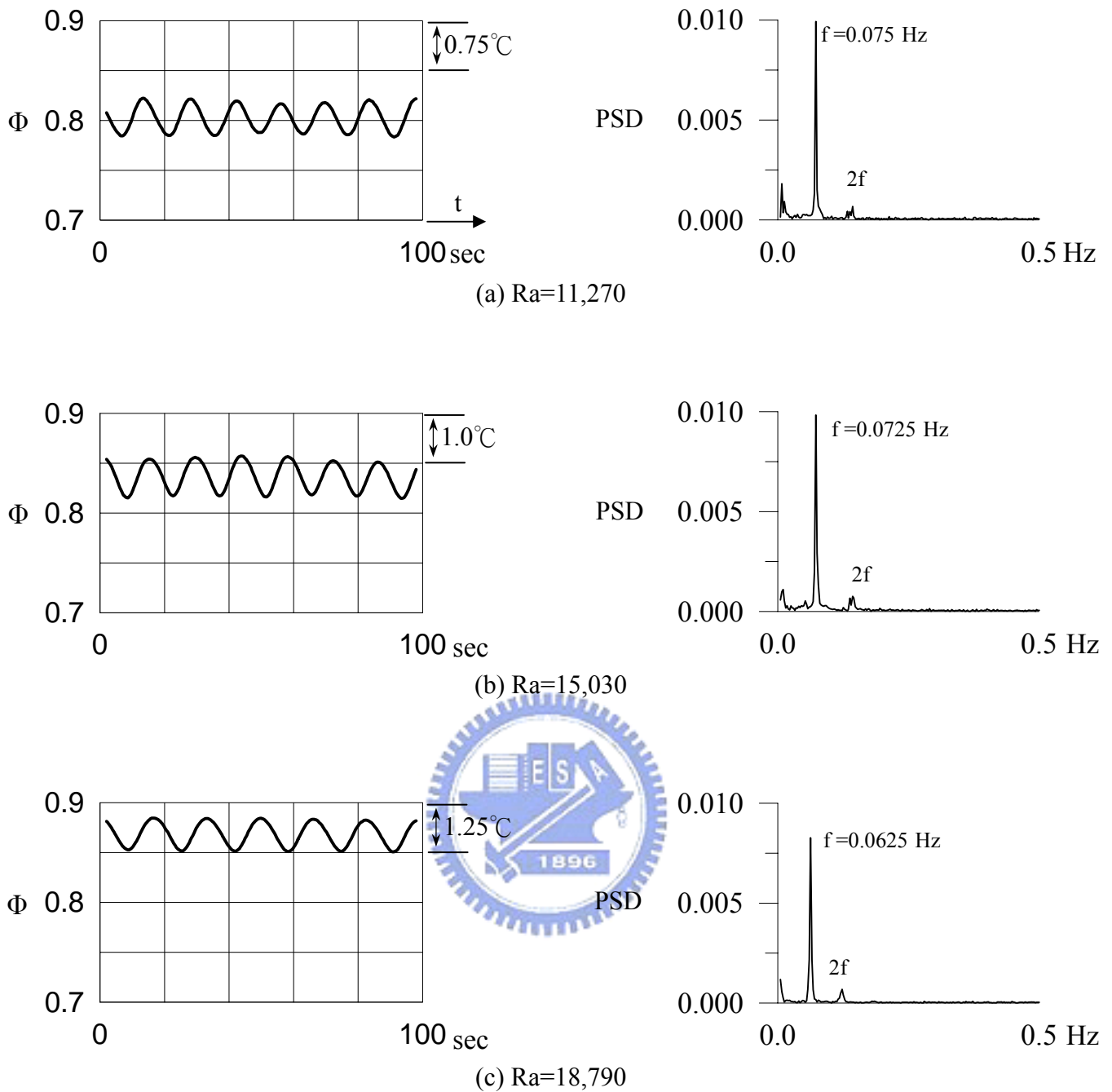
Fig. 4.3   The time records of non-dimensional air temperature and corresponding power spectrum densities for Re_j=61 and D_j=22.1 mm at location (R, Z) =(0.52, 0.5) for θ=0° with H=20.0 mm for various Rayleigh numbers Ra= (a) 11,270, (b) 15,030 and (c) 18,790.
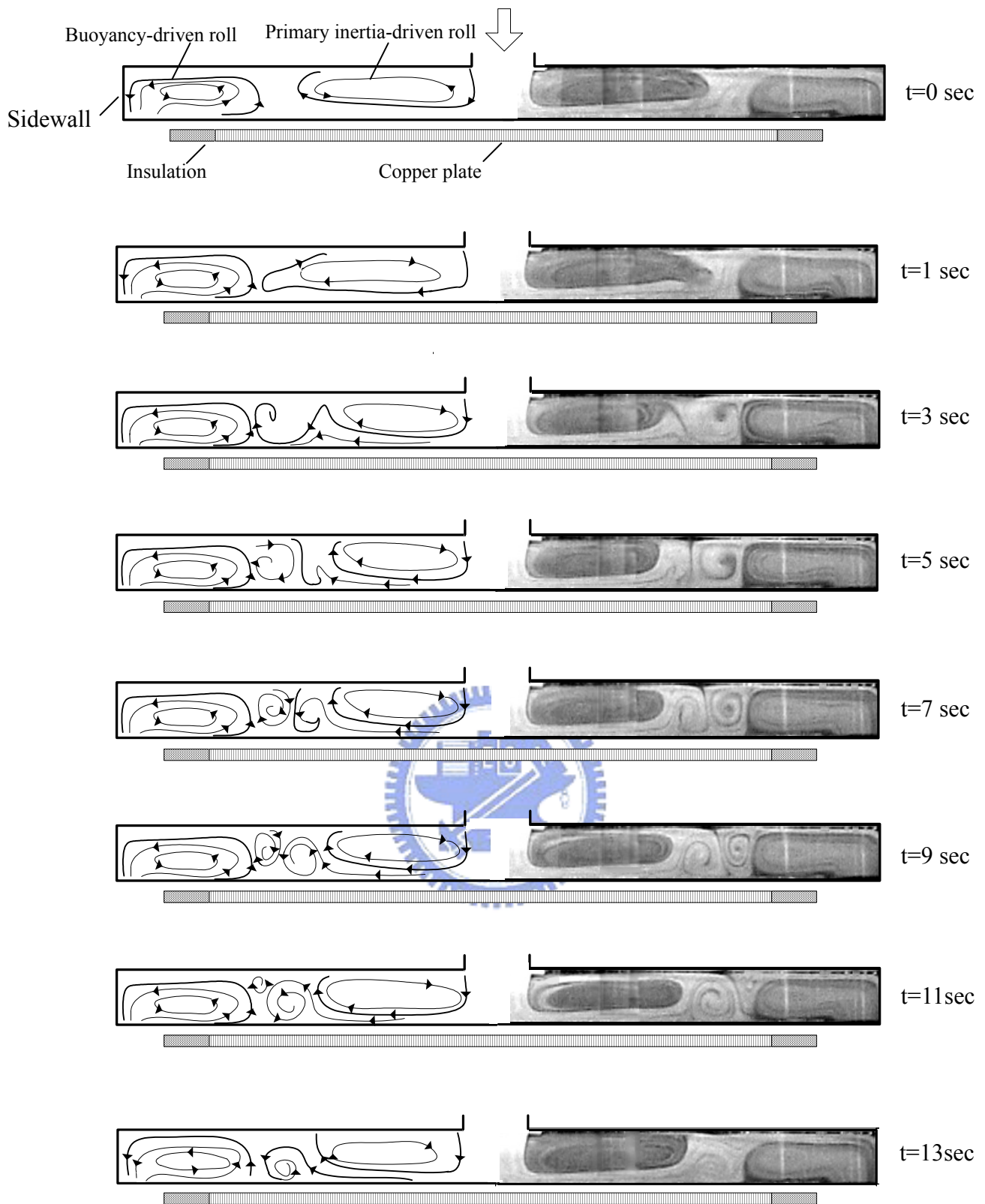
Fig. 4.4 Side view flow photos taken at the cross plane $\theta = 0°$ for $Re_j=61$, Ra=11,270 and D_j=22.1 mm with H=20.0 mm at selected time instants (right) and the corresponding schematically sketched cross plane flow (left) in a typical periodic cycle (t_p=13.3sec).
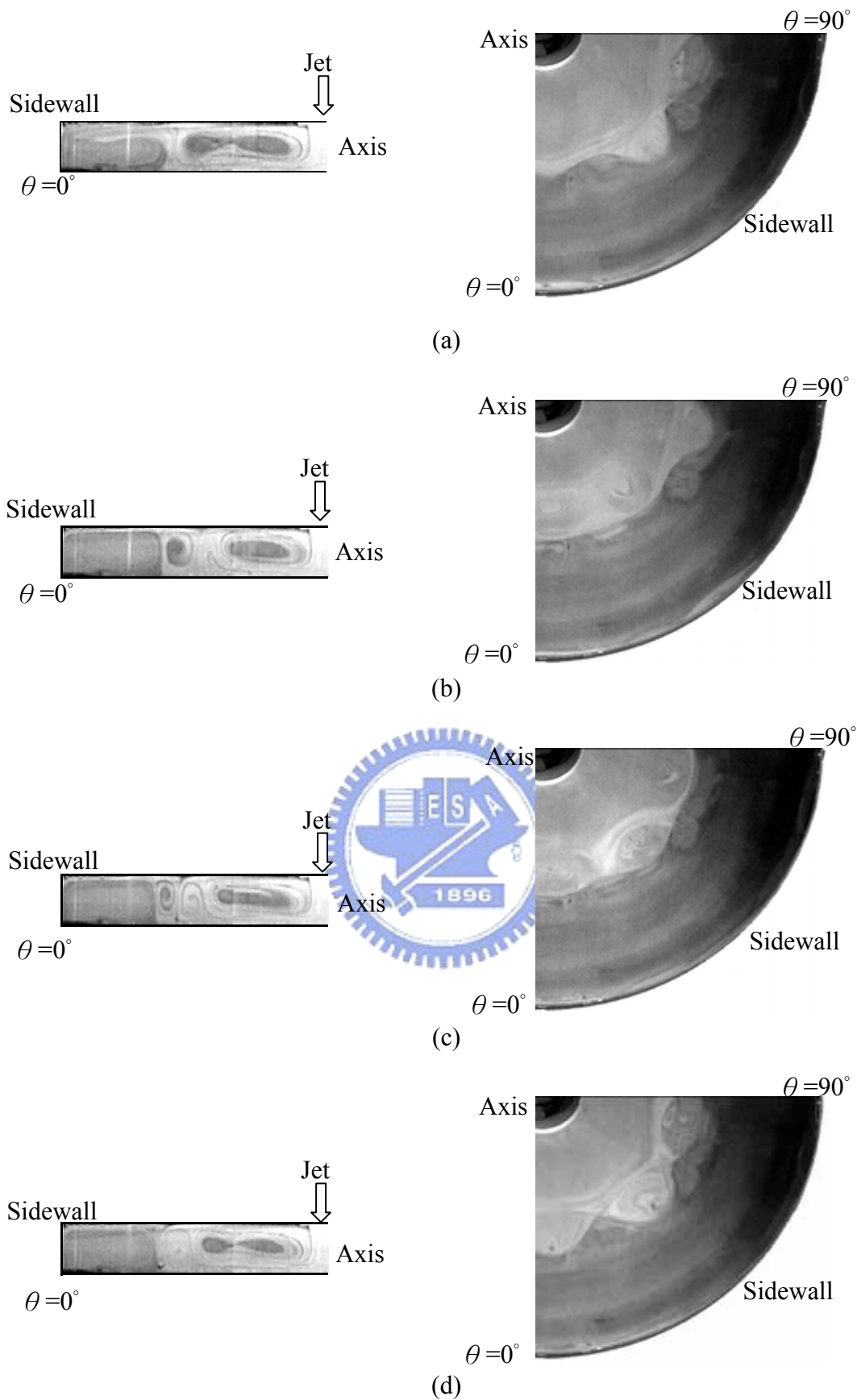
Fig. 4.5 Half side view flow photos taken at $\theta = 0°$ (left) and quarter of top view flow photos (right) taken at midheight of the chamber with $Re_j = 61$, $Ra = 11,270$ and $D_j = 22.1$ mm for $H = 20.0$ mm at selected time instants in statistical state for (a) t=0 sec, (b) t=5 sec, (c) t=9 sec and (d) t=13 sec.
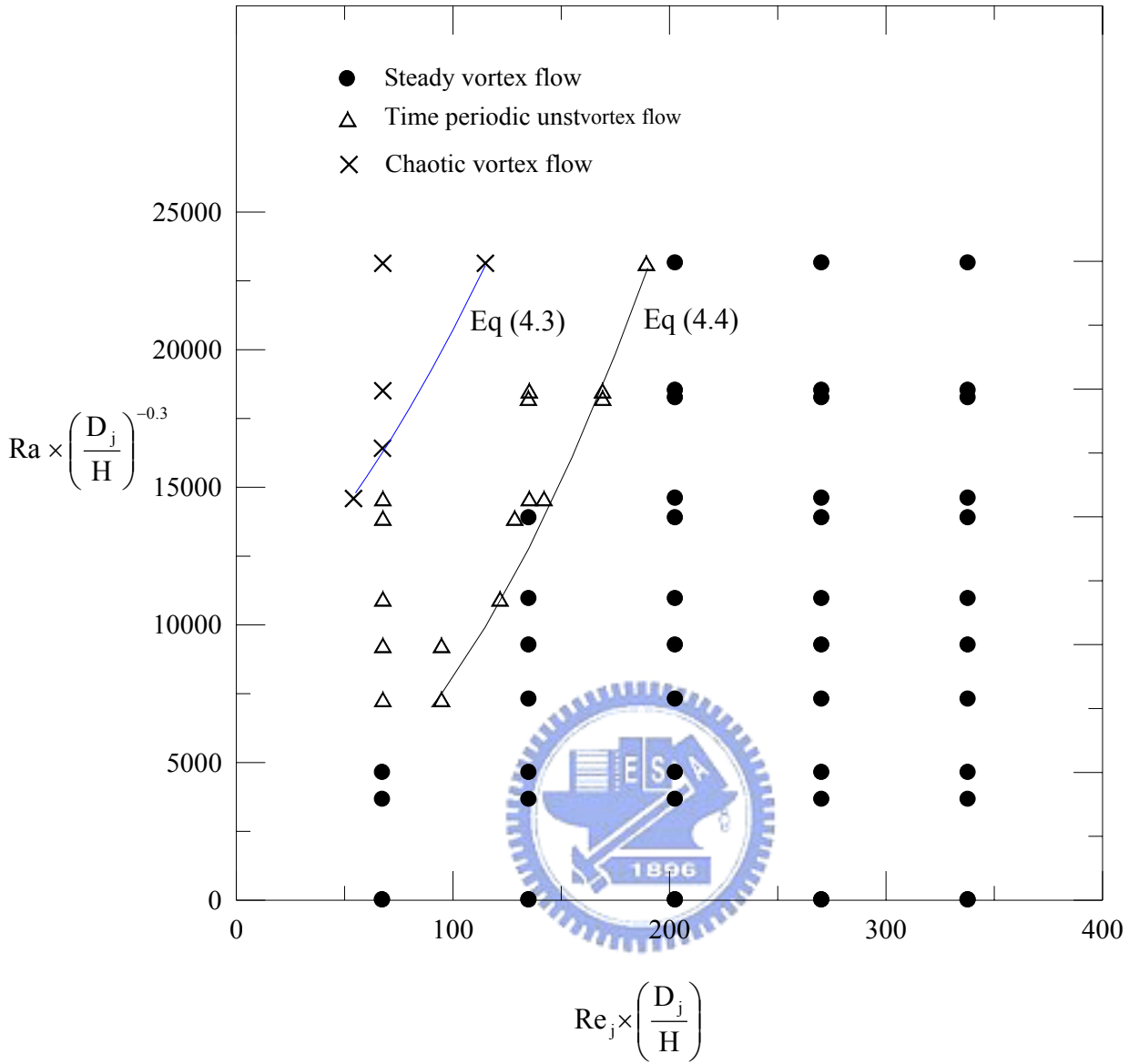
Fig. 4.6   Flow region map delineating the temporal state of the vortex flow for H=20.0 mm.
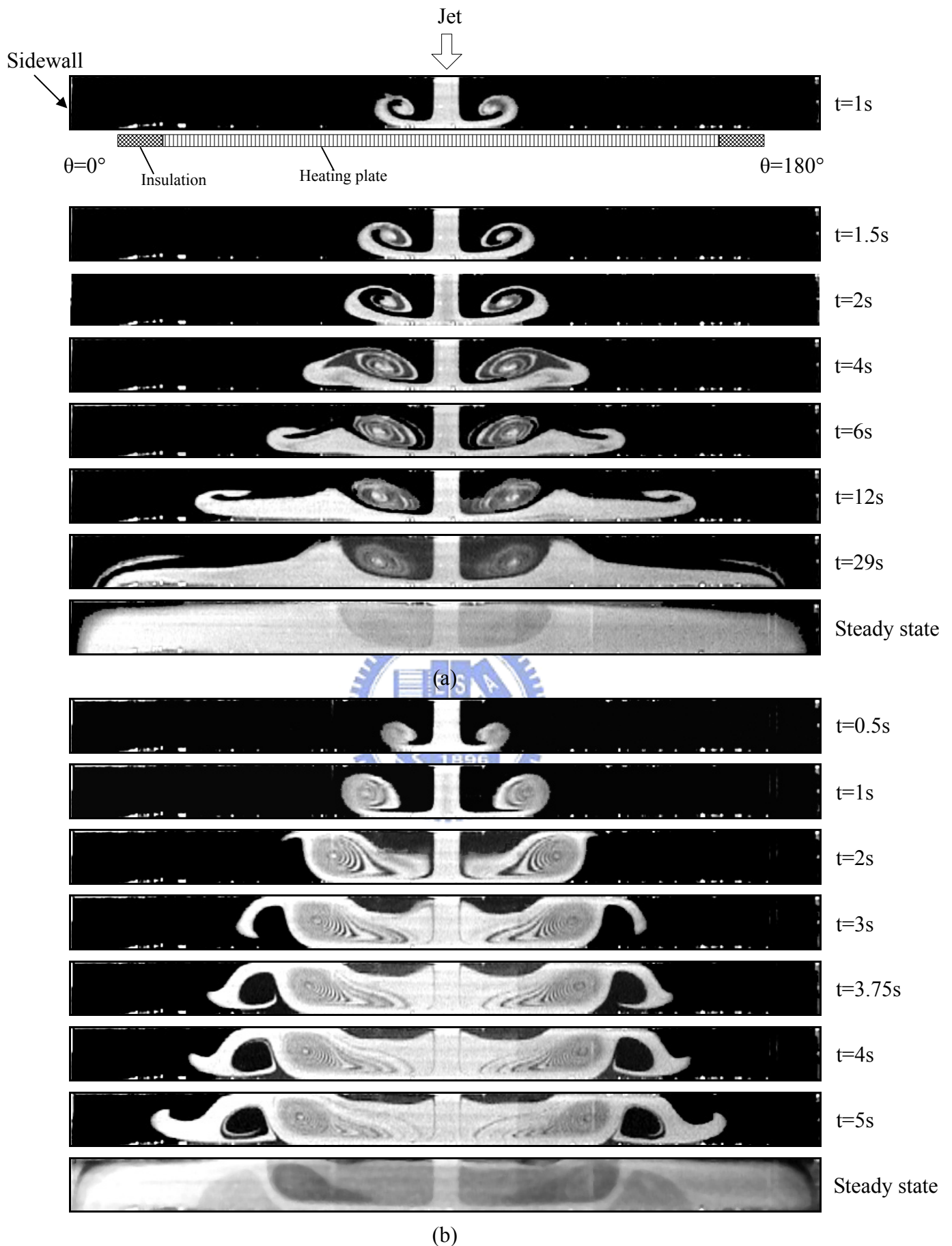
Fig. 4.7   The side view flow photos at selected time instants during flow formation
at the cross plane θ =0° & 180° for Ra=0 at H=20.0 mm & D_j=10.0 mm
for Re_j= (a) 136 and (b) 676.
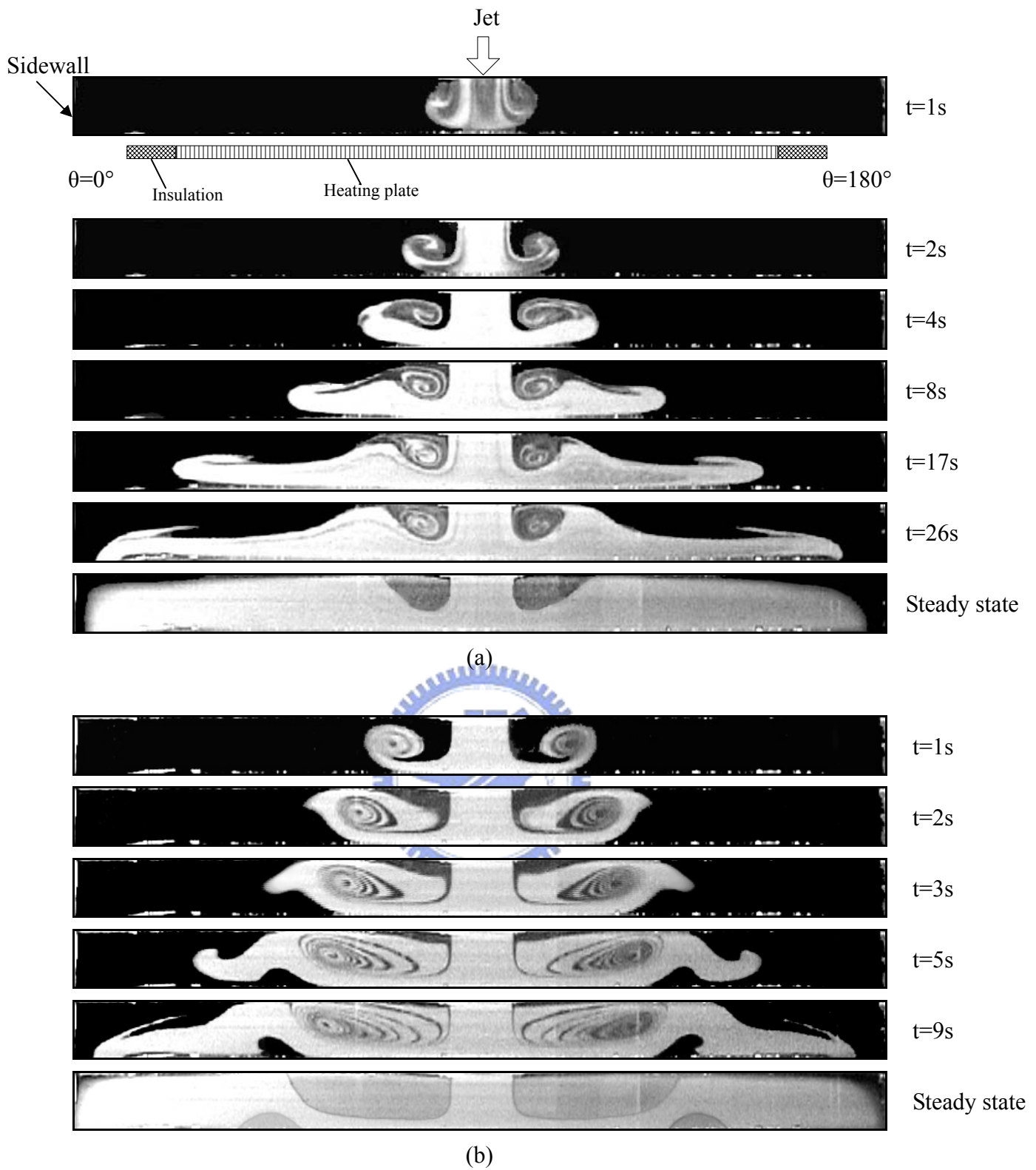
Fig. 4.8   The side view flow photos at selected time instants during flow formation
at the cross plane θ =0° & 180° for Ra=0 at H=20.0 mm & D_j=22.1 mm
for Re_j= (a) 61 and (b) 306.
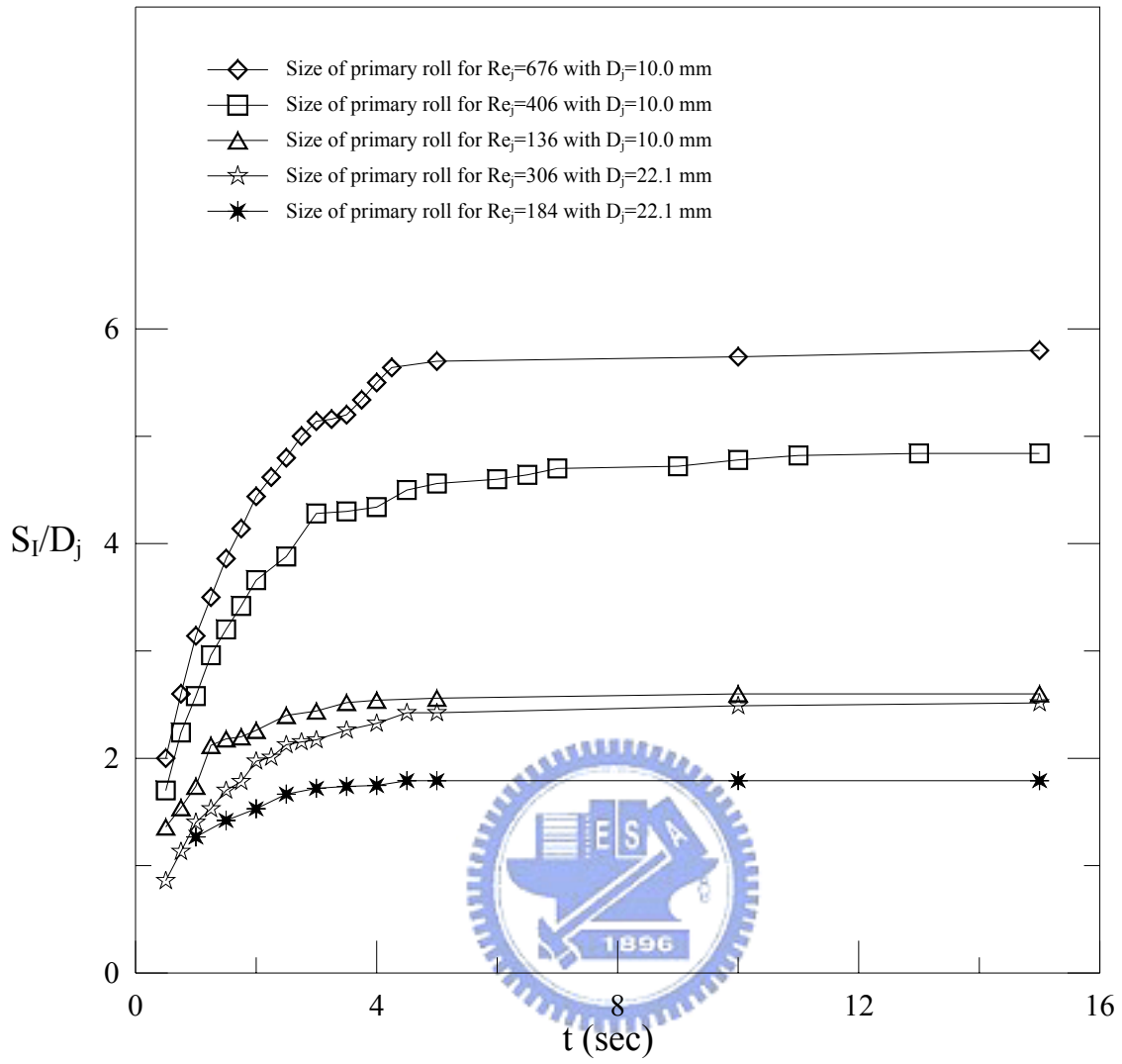
Fig. 4.9   Time variation of the size of the primary inertia-driven roll for various Re_j at Ra=0.
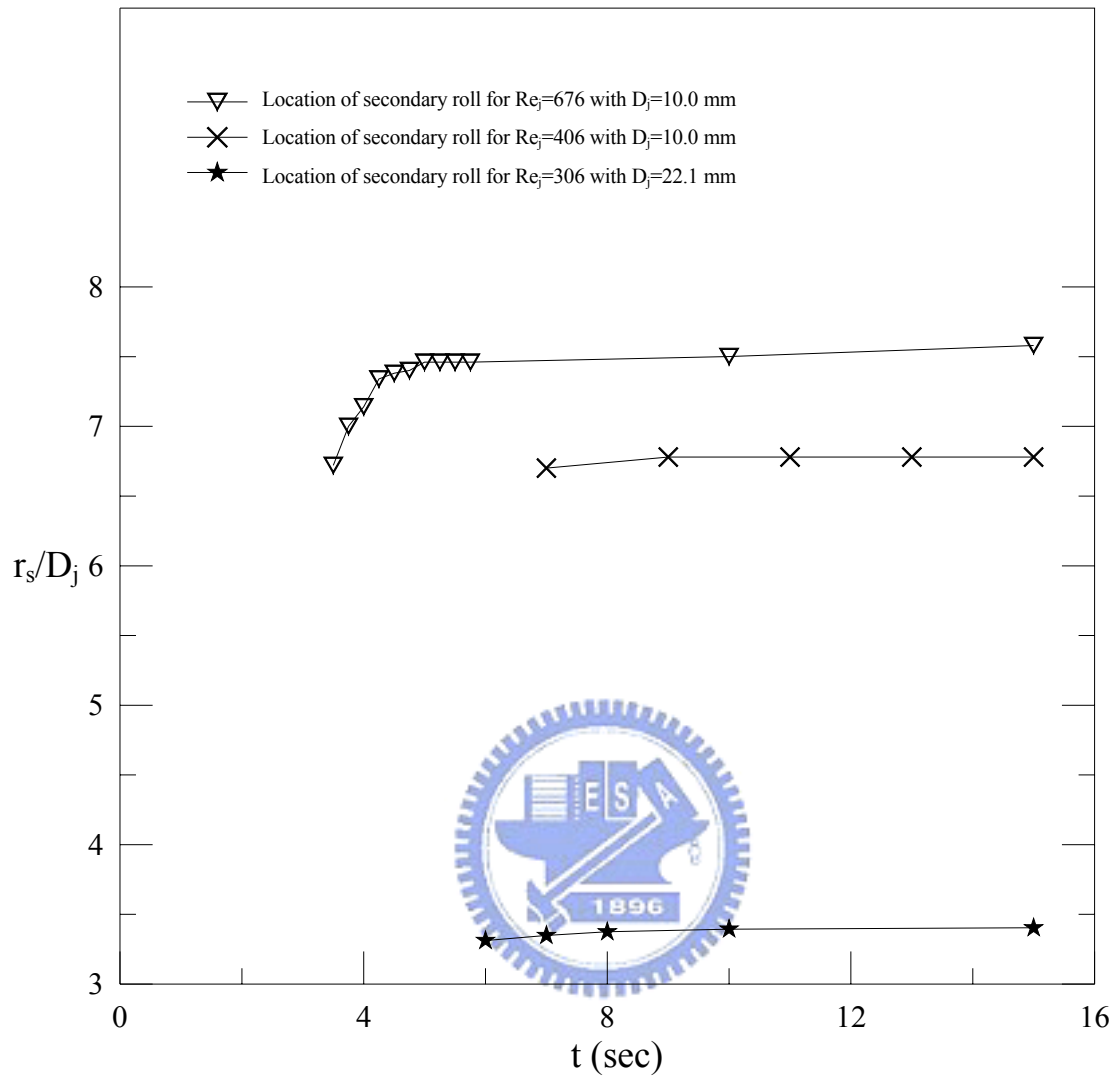
Fig. 4.10 Time variation of the location of the secondary inertia-driven roll for various Re_j at $Ra=0$.